Title

Heterogeneous field response of hierarchical polar laminates in relaxor ferroelectrics

Journal

Science, 384(6703)

ISSN

0036-8075

Authors

Zheng, Hao

Zhou, Tao

Sheyfer, Dina

et al.

Publication Date

2024-06-28

DOI

10.1126/science.ado4494

Heterogeneous field response of hierarchical polar laminates in relaxor ferroelectrics

Hao Zheng[1,2]*, Tao Zhou[3], Dina Sheyfer[2], Jieun Kim[4], Jiyeob Kim[4], Travis D. Frazer[1‡], Zhonghou Cai[2], Martin V. Holt[3], Zhan Zhang[2], J. F. Mitchell[1], Lane W. Martin[4,5,6]*, and Yue Cao[1]*

[1] Materials Science Division, Argonne National Laboratory; Lemont, IL 60439, USA.
[2] X-ray Science Division, Argonne National Laboratory; Lemont, IL 60439, USA.
[3] Center for Nanoscale Materials, Argonne National Laboratory; Lemont, IL 60439, USA.
[4] Department of Materials Science and Engineering, University of California Berkeley; Berkeley, CA 94720, USA.
[5] Materials Sciences Division, Lawrence Berkeley National Laboratory; Berkeley, CA 94720, USA.
[6] Departments of Materials Science and NanoEngineering, Chemistry, and Physics and Astronomy and Rice Advanced Materials Institute, Rice University, Houston, TX 77005, USA.

‡ Present address: KMLabs, Boulder, CO 80301, USA
* For further information: hao.zheng@anl.gov (H.Z.), lwmartin@rice.edu (L.W.M.), yue.cao@anl.gov (Y.C.)

Abstract

Understanding the microscopic origin of the superior electromechanical response in relaxor ferroelectrics requires knowledge not only of the atomic-scale formation of polar nanodomains (PNDs) but more importantly the rules governing the arrangements and stimulated response of PNDs over longer distances. Using X-ray coherent nano-diffraction, we show the staggered self-assembly of PNDs into unidirectional mesostructures that we refer to as polar laminates in the relaxor ferroelectric $0.68PbMg_{1/3}Nb_{2/3}O_3$-$0.32PbTiO_3$ (PMN-0.32PT). We reveal the highly heterogeneous electric-field-driven responses of intra- and inter-laminate PNDs and establish their correlation with the local strain and the nature of the PND walls. Our observations highlight the critical role of hierarchical lattice organizations on macroscopic material properties and provide a guiding principle for the understanding and design of relaxors and a wide range of quantum and functional materials.

One-Sentence Summary:

Mesoscale self-assembly of nanodomains into polar laminates underlies the superior electromechanical response of relaxor ferroelectrics.

Introduction

The properties of crystalline materials and their responses under external stimuli are determined by their structures across the relevant length scales. Classically, the types of responses a material manifests are defined by the combination of atomic- (*i.e.*, at the 0.01-1 nm length scale) and micro-structures (*e.g.*, grain structure at the 1,000-100,000 nm length scale). In a wide range of materials, however, additional complexity can arise from mesoscopic interactions between those length scales. For example, spatial heterogeneities were observed across a wide range of quantum materials, where nanoscale lattice deformations deviate from the average atomic structure (1-5). How these spatial heterogeneities impact local and macroscopic material properties in response to external stimuli remains largely elusive. This missing link is important for fully understanding the structure-property relationships and requires the use of spatially resolved measurements under operando conditions.

Relaxor ferroelectrics are one of the most iconic examples of structural heterogeneous materials due to their exceptional dielectric properties associated with spatially inhomogeneous charge polarization. In contrast to other ferroelectrics, relaxor ferroelectrics feature highly sensitive strain response under external electric fields across several orders of magnitude, with an almost negligible hysteresis polarization-electric field (P-E) loop (6-10). The piezoelectric response is most prominent near the morphotropic phase boundary (MPB) where the lattice should be considered as a solid solution of different space-group symmetries (1, 11-13). X-ray (14-22) and neutron (20, 23-30) based scattering experiments revealed that not only does the unit-cell structure evolve in the form of charge polarization rotation and space group symmetry change, but that this atomic-structural change is intimately connected to the local polar order on the scale of 5-10 nm, corresponding to the formation of polar nanodomains (PNDs) (31-38). Understanding the relaxor behavior has mostly been focused on the interplay between the atomic structure and the PNDs (14-38). In contrast, little attention has been given to longer-range interactions between 10-1,000 nm (39-42). In particular, determining if interactions among the PNDs are important has not been demonstrated. For the majority of ferroelectrics that have micron-sized domains, the inter-domain interactions and the free energy of the domain walls are critical to the stabilization of the ferroelectric order and the macroscopic electric field response. This drives questions about how the PNDs are spatially arranged over larger length scales and if the arrangement enhances the electromechanical response under electric field in actual devices.

Using operando coherent nano-diffraction (CND) (43), we reveal the emergence of mesoscale lattice order that we refer to as "polar laminates" in the canonical relaxor ferroelectric $0.68PbMg_{1/3}Nb_{2/3}O_3$-$0.32PbTiO_3$ (PMN-0.32PT). These laminates have a size of ~350 nm and arise from the staggered arrangement of ~13 nm monoclinic PNDs along the <110> of the pseudocubic lattice. The spatial distribution of *c*-axis strain is directly correlated with the tilting of the PNDs and is most prominent between the laminates. We conducted additional operando CND studies that demonstrate heterogeneous electric-field-driven responses. The most active regions tend to reside inside the laminates while the spatial pinning centers are between the laminates. Our observation reveals the hierarchical assembly of lattice order as a different form of electron and lattice self-organization in heterogenous materials and establishes the role of such mesoscale spatial arrangement in connecting the nanoscale heterogeneity and macroscopic material properties. Our discovery provides a guiding principle for the design and optimization of relaxors and may be important for a wider range of quantum and functional materials.

PMN-0.32PT thin films built from monoclinic PNDs

The PMN-0.32PT we studied belongs to a larger family of the canonical relaxor ferroelectric $(1-x)PbMg_{2/3}Nb_{1/3}O_3$-$(x)PbTiO_3$ (PMN-*x*PT) and resides in the proximity to the MPB. We synthesized thin films of PMN-0.32PT on $SmScO_3$ (SSO) $(110)_o$ substrates (where the "o" denotes orthorhombic indices) with a 25 nm $Ba_{0.5}Sr_{0.5}RuO_3$ (BSRO) bottom electrode (44). We grew a second 25 nm BSRO layer in situ on top of the PMN-0.32PT and fabricated into circular capacitor structures to serve as the top electrode for electric-field-driven studies (Fig. 1A) (45,46). We obtained the average lattice structure of the BSRO/PMN-

0.32PT/BSRO/SSO $(110)_o$ heterostructures from reciprocal space mapping (RSM) about the 002_{pc}-Bragg peak (where "pc" denotes pseudocubic indices) acquired using parallel X-ray beams (Fig. 1B and C) (45). We labeled the Miller indices H, K, and L, using the pseudocubic lattice parameters of the SSO substrate with $c_{SSO,pc}$ = 3.992 Å. Unless otherwise noted, the lattice parameters we discuss are those of the PMN-0.32PT. We found the 002_{pc}-Bragg peak of the PMN-0.32PT at L = 1.95, corresponding to an average lattice parameter c_{pc} = 4.098 Å, slightly longer than that of the bulk crystal (45). This elongation comes from the small compressive strain in plane due to epitaxial growth on the SSO substrate. Despite a minor in-plane anisotropy (a_{pc} = 3.991 Å and b_{pc} = 3.983 Å), the diffuse scattering of the PMN-0.32PT about the 002_{pc}-Bragg peak is essentially isotropic in the film plane (Fig. 1C). The line profiles of the diffuse-scattering pattern along H and K are both Lorentzians with a full-width-at-half-maximum (FWHM) of 0.075 nm^{-1} (Fig. 1D), corresponding to a correlation length of ~13.4 nm which can be taken as the characteristic size of the PNDs in the film plane. Further analysis of the diffuse-scattering pattern revealed that the average-atomic structure of the PMN-0.32PT in the heterostructure is monoclinic (M_c), consistent with previous reports (44). On the length scale of the device (50 μm in diameter), the PNDs are twinned with finite lattice tilts along either $[100]_{pc}$ or $[010]_{pc}$ deviating from 90° (Fig. 2, A to C), which we named $\Delta\alpha$ or $\Delta\beta$, respectively.

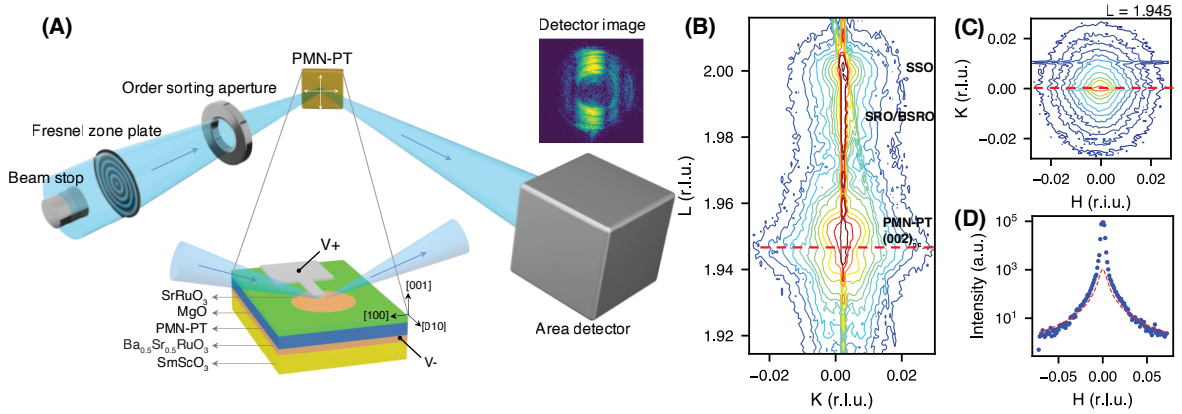

Fig. 1: The PMN-0.32PT thin film device and the experimental setup (A) Sketch of the experimental setup of in-situ X-ray coherent nano diffraction (CND). The electric field is applied along the $[001]_{pc}$ direction. Raster scans using the nanobeam reveal the local domain structure in PMN-0.32PT. Bottom inset: the BSRO/PMN-0.32PT/BSRO/SSO heterostructure. Top inset: A typical nano diffraction pattern from the PMN-0.32PT $(002)_{pc}$ Bragg peak. **(B, C)** H-cut and L-cut from the reciprocal space map of the PMN-0.32PT/BSRO/SSO heterostructure. The miller indices H, K, and L are labeled using the lattice parameters of the SSO substrate. The $(002)_{pc}$ peak of PMN-0.32PT shows an almost circular diffuse scattering pattern. **(D)** Diffuse scattering intensity extracted from the dashed lines in **c**, and red lines show the Lorentz fitting to the profile of the diffuse scattering, i.e., $I = \frac{I_0}{\pi}\frac{\Gamma}{(q-q_0)^2+\Gamma^2}$. A fitted value of Γ=0.075 nm^{-1} is obtained corresponding to a correlation length of 13.2 nm.

Self-assembly of PNDs into polar laminates

We prealigned and mounted the PMN-0.32PT-based capacitor devices in a reflection geometry with the $[001]_{pc}$ and $[100]_{pc}$ in the scattering plane (45). Upstream of the sample, we focused highly coherent 10 keV X-ray photons to a diameter of 25 nm (FWHM) using a Fresnel zone plate, with a convergence angle of 0.5°. We tuned the sample theta and detector two-theta angles to access the 002_{pc}-Bragg reflection of the PMN-0.32PT film. Due to the difference in the *c* lattice constants under the pseudocubic notation, the nano-diffraction intensity comes predominately from the PMN-0.32PT and not from the SSO or BSRO. A typical CND pattern (inset, Fig. 1A) encodes information about the local lattice deformation within the focused X-

ray photon footprint. Analyzing the distribution of diffraction intensity allows for quantification of the local lattice strain ϵ_c and tilts (*i.e.*, $\Delta\alpha$ and $\Delta\beta$) as well as their uncertainties (45,46).

We show typical distributions of ϵ_c , $\Delta\alpha$, and $\Delta\beta$ extracted from the raster scan of a 5 μm × 5 μm field of view (Fig. 2A-C). The spatial distributions of these parameters exhibit three features that are distinct from those in standard ferroelectrics. First, the spatial distribution of the *c*-axis strain ϵ_c is not directly correlated with that of either $\Delta\alpha$ or $\Delta\beta$, in sharp contrast to canonical ferroelectrics [*e.g.*, $BiFeO_3$ (47)]. The lack of direct correlation arises from the small size of the PNDs, and fundamentally reflects the nature of PMN-0.32PT as a solid solution near the MPB. Second, a spatial correlation does exist between the *c*-axis strain and the relative change of the projected lattice tilt $\boldsymbol{v} = (\Delta\beta,\ \Delta\alpha)$. To visualize this, a zoomed-in view of the lattice distortion (2.5 μm ×1 μm) is displayed (upper panel, Fig. 2D). The color map shows the distribution of the divergence $-\nabla\cdot\boldsymbol{v}$ while the arrows represent the projected lattice tilts $\boldsymbol{v}$. We multiplied the prefactor of -1 to the divergence for direct visual comparison with the distribution of ϵ_c over the same area (lower panel, Fig. 2D). Indeed, we obtained a Pearson coefficient r = -0.587 from the correlation plot (Fig. 2E). The correlation between ϵ_c and $\nabla\cdot\boldsymbol{v}$ is nontrivial and highlights the importance of the domain walls between the PNDs. Specifically, local maxima and minima of $\nabla\cdot\boldsymbol{v}$ correspond to the regions where the neighboring $\boldsymbol{v}$ tilts towards opposite (180°) directions. These regions contain domain walls between the twinned monoclinic PNDs. Third, the PNDs self-organize and form a mesoscale lattice order almost parallel to the $<110>_{pc}$. This lattice order is unidirectional, which is best seen from the stripy distribution of $\Delta\alpha$ (Fig. 2B) and of $\Delta\beta$ (Fig. 2C), albeit less clearly in the latter. Admittedly, our observation was made from PMN-0.32PT under moderate epitaxial strain. The detailed morphology of the polar laminates, e.g., the width versus the length of the laminate, and whether or how precisely the laminates extend along $<110>_{pc}$ may be affected by the epitaxial strain. Nonetheless, the correlation between lattice tilts and c-axis strain does not rely directly on the epitaxy itself but instead follows naturally from the detailed interactions between the PNDs and domain walls. It is thus plausible that such a correlation will hold for films from different substrates and potentially for bulk crystals. Similarly, we expect that the heterogeneous operando responses of PNDs, which we will discuss later in the text, to hold beyond the current work.

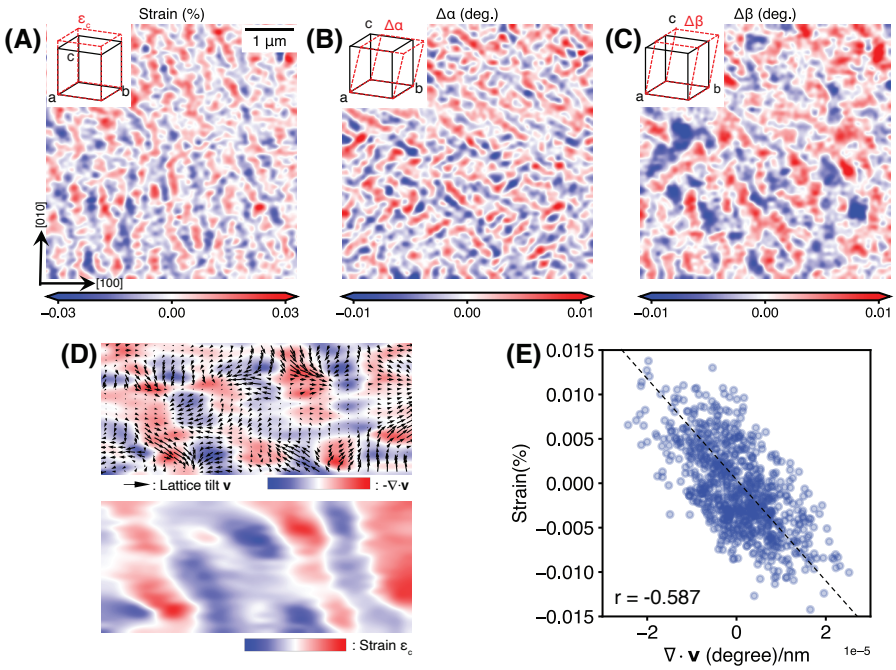

Fig. 2: Mesoscale distributions of the lattice distortions. (**A-C**) The distortion of the c lattice vector away from the average pseudocubic unit cell can be decomposed into three components: strain ε_c, lattice tilt $\Delta\alpha$, and lattice tilt $\Delta\beta$. Spatial distributions of ε_c (**A**), $\Delta\alpha$ (**B**), and $\Delta\beta$ (**C**) were obtained from the CND over a

5 μm × 5 μm area. Schematics of these distortions are displayed in the insets on the top left corner of each map. **(D)** Correlation between strain and the divergence of the projected lattice tilts. Upper panel: projected lattice tilts (arrow) and the calculated divergence (color map). Lower panel: the distribution of measured strain. **(E)** Scatter plot of strain and divergence of lattice tilt. A Pearson correlation coefficient r = -0.587 confirms the correlation between the two quantities.

Further statistical analysis of the projected lattice tilts $\boldsymbol{v}$ revealed that the polar laminates originate from the self-organization of the PNDs. The distribution of $\boldsymbol{v}$ from the same field of view (as in Fig. 2B) is shown (Fig. 3A). Lattice tilts with similar orientations are labeled with like colors and segregate into diagonal patches consistent with our observations of the unidirectional lattice order. Interestingly, a large fraction of the lattice tilts point away from the $<100>_{pc}$, and instead lie along the $<110>_{pc}$ (Fig. 3C). Because the PNDs in PMN-0.32PT are monoclinic M_c (22), the diagonal lattice tilts should be interpreted as the existence of PNDs sharing 90° head-to-head or tail-to-tail domain walls within the X-ray photon footprint (Fig. 3C), with the total charge polarization and lattice tilt along the $<110>_{pc}$. This interpretation is because the focused X-ray beam contains several PNDs within the illuminated volume. Specifically, the incidence angle of the X-ray is 17.5° with an in-plane footprint of 25 nm × 80 nm, ten times larger than the size of the PNDs.

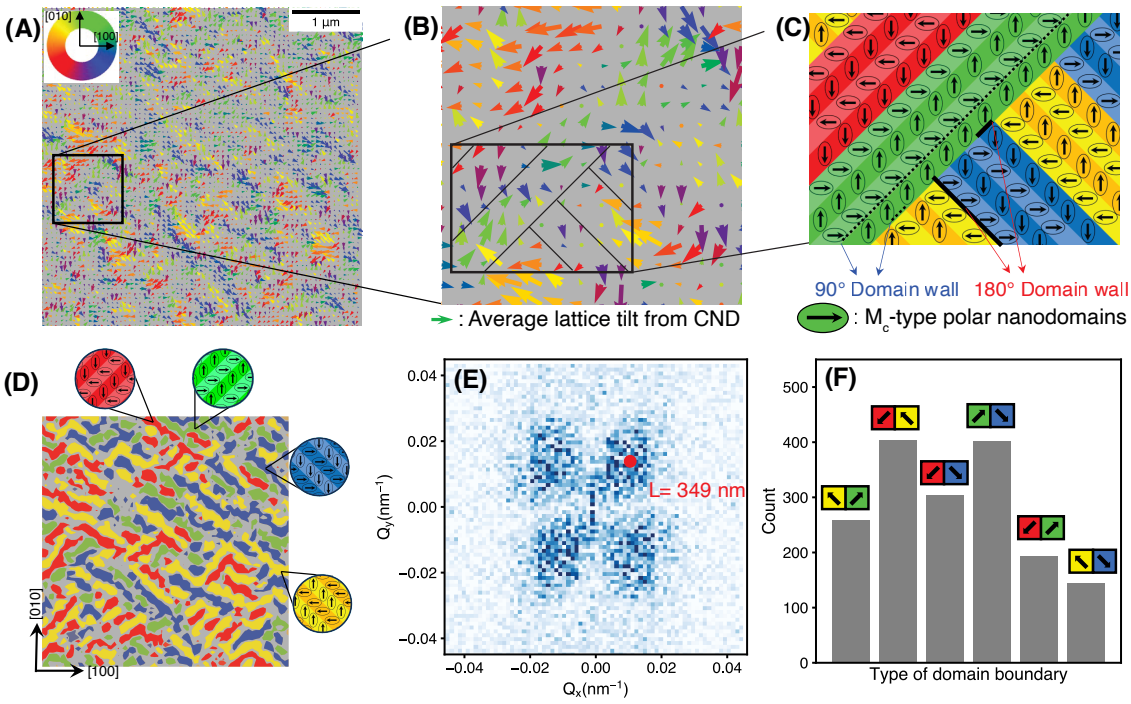

Fig. 3: Unidirectional polar laminates and their relation to PNDs. (A) Vector field representing the spatial distribution of projected lattice tilt from the same area shown in Fig. 2D. The orientations of lattice tilt are labeled with colors indicated in the color wheel. **(B)** A zoomed-in view showing the spatial arrangement of lattice tilts. A polar laminate consists of neighboring sites with similar lattice tilts and tends to align along the diagonal $<110>_{pc}$ directions. **(C)** Cartoon schematic of polar laminates. Inside each laminate, staggered M_c domains with perpendicular polarizations (ovals with black arrows) give rise to the 90° PND walls and extend diagonally. In contrast, boundaries between laminates (solid black lines in both B and C) host a mixture of 90° and 180° PND walls. **(D)** The classification of the polar laminate structure is generated by clustering the lattice tilts. **(E)** Fast Fourier transform of the spatial map shown in **(A)**. The butterfly pattern reveals a four-fold diagonal arrangement of polar laminates with a correlation length of 349 nm. **(F)** Statistics of the boundaries between laminates. There are substantially more boundaries between orthogonal laminates than between antiparallel ones.

We refer to the unidirectional arrangement of PNDs along $<110>_{pc}$ over a continuous region as "polar laminates" (Fig. 3D). These polar laminates are different from previously reported microstructures (*e.g.*, herringbone domains (48-51)) in a few ways. First, each laminate consists of two types of M_c PNDs that are staggered with 90° domain walls, rather than of a singular domain type more common for the herringbones. Second, hierarchically, these polar laminates proliferate in the PMN-0.32PT and serve as the basic building block of the entire material. We arrived at this conclusion after examining many micron-sized fields of view over multiple devices. As we will show later in the operando CND data, these polar laminates exhibit spatially heterogeneous electric-field responses and are vital to the macroscopic electromechanical properties.

We classify the polar laminates into four groups using the experimentally observed lattice tilts and identify their characteristic ordering vector and length scale. A classification of polar laminates can be generated by clustering neighboring sites within $\pm 22.5^\circ$ of four diagonal directions, with each color representing a preferred orientation lattice tilt (Fig. 3D). The predominant orientation of lattice tilt inside the laminate is labeled using different colors (Fig. S8**)**. Here, green, yellow, red, and blue colors represent preferred lattice tilts along the $[110]_{pc}$, $[\bar{1}10]_{pc}$, $[\bar{1}\bar{1}0]_{pc}$, and $[1\bar{1}0]_{pc}$, respectively. The two-dimensional fast Fourier transform (FFT) of the laminate distribution has a characteristic ordering wavevector centered at Q = (0.012, 0.014, 0) nm^{-1} (Fig. 3E), corresponding to a length scale of ~350 nm in the sample plane characteristic of the polar laminates. The large length scale, well over 100 nm, prevented these polar laminates from being directly resolved in the RSMs due to the limited momentum resolution. Finally, the direction of Q deviates slightly from the $[110]_{pc}$, possibly because of the minor difference between the lattice constants a_{pc} and b_{pc} in the plane.

Following the classification, we identified six types of inter-laminate boundaries. We provide a histogram of these boundaries from the field of view used previously (Fig. 3A, F). Several notable observations about the boundaries are worth discussing. First, boundaries between orthogonal laminates are preferred compared to those between antiparallel laminates. This orientational preference comes from the nature of the inter-laminate domain walls. Specifically, while the intra-laminate PND walls are entirely 90° head-to-head, the orthogonal inter-laminate boundaries consist of alternating 90° and 180° PND walls (Fig. 3C). As the 180° domain walls are generally considered as higher in energy than the 90° walls (52), the boundaries between laminates are expected to be "harder" and less likely to move than the intra-laminate PND walls under an electric field. Second, the inter-laminate boundaries can be categorized into two groups with 180° PND walls along the $[100]_{pc}$ (yellow-green and red-blue boundaries) and $[010]_{pc}$ (red-yellow and blue-green boundaries), respectively. The group with PND walls along the $[100]_{pc}$ have a slightly higher population, possibly due to the in-plane anisotropy from the SSO substrate epitaxy.

The discovery of such polar laminates reveals a different kind of hierarchical spatial heterogeneity in relaxors and provides key insights into the interactions between PNDs. Specifically, individual atoms packed in ~ 0.4 nm unit cells form ~13 nm monoclinic PNDs, which subsequently assemble into polar laminates ~350 nm in size. Most intriguingly, these polar laminates are further organized in an almost self-similar manner, which is evidenced by the FFT (Fig. 3E) and is reminiscent of the diffuse scattering in PMN-0.30PT (21). This observation amounts to direct evidence that the PNDs and the polar laminates are hierarchically ordered over many magnitudes of lengths scales. Moreover, the formation of polar laminates highlights the cooperative interactions between PNDs. The dominance of 90° PND walls sharply contrasts that in typical ferroelectric materials and lowers the contribution of domain walls to the total free energy in relaxors due to the small domain size and the large number of domain walls.

Highly heterogeneous electric field response of PNDs

The discovery of polar laminates provides the basis for revealing and understanding the spatially heterogeneous field response of PMN-0.32PT. To do this, we performed operando CND under a DC electric

field sequence of the form: 0 kV·cm^{-1} → +540 kV·cm^{-1} → -540 kV·cm^{-1} → 0 kV·cm^{-1}. At each applied field, raster scans were performed to track the nanoscale evolution of lattice distortions (45) (Fig. S9). We display the distributions of ϵ_c and $\boldsymbol{v} = (\Delta\beta,\ \Delta\alpha)$ from a 2.5 μm × 2.5 μm field of view (Fig. 4A1 and B1). The relative strain distribution in the film plane generally stays intact under different electric fields (Fig. S9), indicating strong spatial pinning of the PNDs. Such an effect is also evidenced by the evolution of the average strain along the field cycle. The strain averaged over the entire field of view exhibits a butterfly shape (Fig. 4C) consistent with macroscopic property measurements. The butterfly loop is asymmetric relative to the field direction, with a more pronounced strain response under the negative bias. Such asymmetry was also observed in the polarization loop (Fig. S2) as well as from other PMN-0.32PT devices we measured, possibly due to the asymmetric layouts of the top and bottom electrodes.

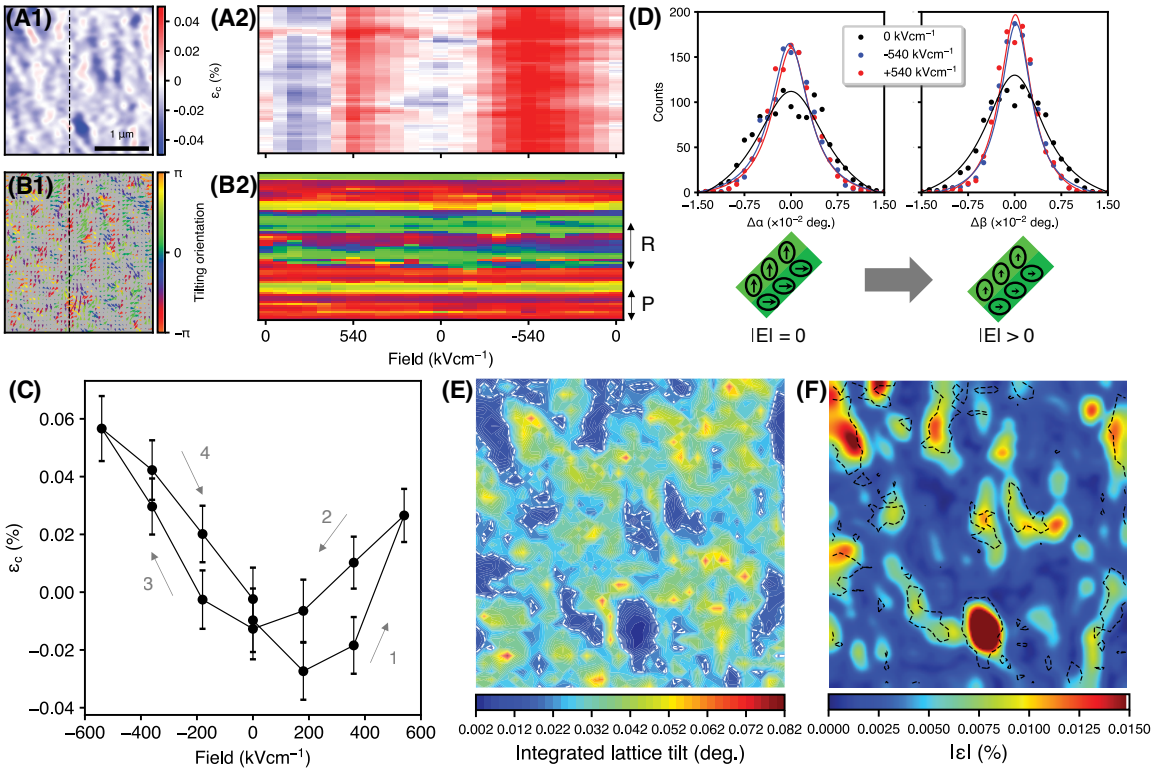

Fig. 4: Electric-field driven evolution of the polar laminates. (A1) Strain distribution derived from in-situ CND scans on a 2.5 μm × 2.5 μm area at E = 0 kV·cm^{-1}. **(A2)** Waterfall plot shows the voltage dependence of strain in a column of pixels (dashed line in **(A1)**) during a cycle of field 0 kVcm^{-1} → +540 kV·cm^{-1} → 0 kV·cm^{-1} → -540 kV·cm^{-1} → 0 kV·cm^{-1} applied along the $[001]_{pc}$ direction. **(B1)** Map of projected lattice tilts from the same area. The orientation of projected lattice tilt is labeled with colors. The tilt angle is zero when the projected tilt is parallel to the $[100]_{pc}$ direction. **(B2)** Evolution of the orientation of projected lattice tilts from the same area. "P" and "R" correspond to the pinned and responsive regions, respectively. **(C)** Spatially averaged strain as a function of the applied electric field generated from the same area. The standard deviation of strain at each field is indicated by the error bar. **(D)** Statistics of lattice tilts $\Delta\alpha$ (upper left) and $\Delta\beta$ (upper right) at 0 kV·cm^{-1} and ±540 kV·cm^{-1}. The electric field along the $[001]_{pc}$ direction induces a decrease of lattice tilts projected onto the sample plane, corresponding to a transition from the monoclinic to the orthorhombic lattice structure in PNDs (lower row). **(E)** The cumulative change of the projected lattice tilts. Red and blue colors represent the most and the least responsive regions. Dashed contours indicate the distribution of an intermediate integrated lattice tilt of 0.03 degree. **(F)** Spatial distribution of the absolute value of strain. An anti-correlation can be observed between strain and the response of the lattice tilts.

We further survey the evolution of the lattice tilts over the field cycle. On average, the electric field drives the lattice from the monoclinic M_c phase towards the orthorhombic phase, consistent with the field-driven evolution of the average atomic structure (22). We provide histograms of the projected lattice tilts (upper panels, Fig. 4D). With increased electric field, the average lattice tilts shift towards the center where $\Delta\alpha = \Delta\beta = 0$ (*i.e.*, an orthorhombic phase). Detailed inspection of the lattice-tilt evolution during the field cycle uncovers the highly heterogeneous field response. We took one-dimensional cuts of strain and projected lattice tilts from the data (black lines, Fig. 4A1 and B1) and they are stacked as a function of the field cycle into "waterfall" plots. While the field response of strain is relatively uniform (Fig. 4A2), the change in lattice tilts is inhomogeneous (Fig. 4B2). Specifically, some regions of material remain unchanged in the entire cycle, while other regions show a vigorous response to the field. We labeled the two types of regions as pinned (P) and responsive (R) (Fig. 4B2).

Establishing a local link between strain and electromechanical response

Whether a region is responsive or pinned depends strongly on the local lattice strain under the field-free state. To quantify the cumulative response, we integrated the absolute change of the projected lattice tilt $\sum_i |\boldsymbol{v}(E_{i+1}) - \boldsymbol{v}(E_i)|$ over the entire field cycle (Fig. 4E) with the red and blue colors corresponding to the most and least responsive regions, respectively. We also calculated the absolute value of the strain distribution (Fig. 4F) and we found a clear anticorrelation between the dynamic field-induced lattice tilts and the static-strain distribution, where regions with the most pronounced change in lattice tilts have the least strain. The anticorrelation we observed demonstrates the spatial heterogeneity of the electromechanical response and sheds light on the origin of the relaxor behavior. The strain maxima or minima have a larger divergence of lattice tilts (Fig. 2D) corresponding to the boundaries between polar laminates. These regions serve as pinning points during the field cycle. In contrast, areas with smaller strain are more likely to be inside the laminate with 90° PNDs and are substantially more responsive under electric field. Nanoscopically, inside the polar laminates, the aforementioned cooperative lattice-tilt rotation from the M_c to the orthorhombic phase (22,53) reduces the energy on the 90° domain walls, allowing them to be more responsive under the electric field.

The dramatic difference between intra- and inter-laminate domain walls is striking and highlights the need for spatially resolving the local material properties in the presence of heterogeneity. The fact that not all PND walls respond alike to the electric field requires experimentally and theoretically sampling a sufficiently large field of view containing a statistically significant number of domain walls, which is often either not feasible or a missed opportunity in previous studies. Our findings were made possible by the high spatial resolution, high sensitivity to the material property (lattice deformation in our case), and the large field of view combined with the application of electric field during our experiment.

Conclusion and perspectives

In summary, operando CND studies revealed the existence of hierarchical polar laminates in PMN-0.32PT as well as their role in the field-induced relaxor response. The polar laminates arise from the hierarchical self-organization of twinned monoclinic PNDs separated by 90° domain walls. The boundaries between laminates consist of alternating 90° and 180° domain walls, leading to maxima and minima of strain distribution as well as the divergence of local lattice tilts. The operando nano-diffraction studies further established a direct connection between the heterogeneous field response and the detailed structure of the polar laminates. The regions inside the laminates are the most active while the inter-laminate boundaries are spatially pinned due to the presence of the 180° PND walls.

The discovery of polar laminates underscores the cooperation between PNDs in facilitating the electromechanical response and sets up a connection between the nanoscale lattice heterogeneity and the macroscopic material properties. As such, our observations provide a guiding principle for the design and

optimization of future relaxors (54-56). Specifically, we show that the size of the polar laminates governs the population and density of intra- and inter-laminate PND walls, and that the inter-laminate PND walls are more likely to be pinned and less responsive to the electric fields. Therefore, it is imperative to tailor the macroscopic electric field response via strain and defect engineering. For example, the position and density of high-strain regions could be modulated locally via ion implantation or electron beam illumination either directly of the relaxor material or of the underlying substrates. The approach developed herein, including operando CND and the associated analysis, is further applicable to a wide range of quantum and functional materials. Our observations should drive interest in further understanding the role of spatial inhomogeneities in a broad class of materials.

References

1. A. A. Bokov, Z.-G. Ye, Recent progress in relaxor ferroelectrics with perovskite structure. *J. Mater. Sci.* **41**, 31–52 (2006).
2. J. H. E. Cartwright, A. L. Mackay, Beyond crystals: the dialectic of materials and information. *Phil. Trans. R. Soc. A.* **370**, 2807–2822 (2012).
3. D. A. Keen, A. L. Goodwin, The crystallography of correlated disorder. *Nature* **521**, 303–309 (2015).
4. S. J. L. Billinge, I. Levin, The Problem with Determining Atomic Structure at the Nanoscale. *Science* **316**, 561–565 (2007).
5. E. Dagotto, Complexity in Strongly Correlated Electronic Systems. *Science* **309**, 257–262 (2005).
6. S. W. Choi, R. T. R. Shrout, S. J. Jang, A. S. Bhalla, Dielectric and pyroelectric properties in the $Pb(Mg_{1/3}Nb_{2/3})O_3$-$PbTiO_3$ system. *Ferroelectrics* **100**, 29–38 (1989).
7. R. A. Cowley, S. N. Gvasaliya, S. G. Lushnikov, B. Roessli, G. M. Rotaru, Relaxing with relaxors: a review of relaxor ferroelectrics. *Adv. Phys.* **60**, 229–327 (2011).
8. G. A. Smolenskii, A. I. Agranovskaya, Dielectric polarization of a number of complex compounds. *Phys. Solid State* **1**, 1429-1437 (1959).
9. L. E. Cross, Relaxorferroelectrics: An overview. *Ferroelectrics* **151**, 305–320 (1994).
10. A. A. Bokov, Z.-G. Ye, Dielectric relaxation in relaxor ferroelectrics. *J. Adv. Dielectr.* **02**, 1241010 (2012).
11. E. Sun, W. Cao, Relaxor-based ferroelectric single crystals: Growth, domain engineering, characterization and applications. *Prog. Mater. Sci.* **65**, 124–210 (2014).
12. Z.-G. Ye, M. Dong, Morphotropic domain structures and phase transitions in relaxor-based piezo-/ferroelectric $(1-x)Pb(Mg_{1/3}Nb_{2/3})O_3-xPbTiO_3$ single crystals. *J. Appl. Phys.* **87**, 2312–2319 (2000).
13. F. Li, D. Lin, Z. Chen, Z. Cheng, J. Wang, C. Li, Z. Xu, Q. Huang, X. Liao, L.-Q. Chen, T. R. Shrout, S., Zhang, Ultrahigh piezoelectricity in ferroelectric ceramics by design. *Nat. Mater.* **17**, 349–354 (2018).
14. H. You, Q. M. Zhang, Diffuse X-Ray Scattering Study of Lead Magnesium Niobate Single Crystals. *Phys. Rev. Lett.* **79**, 3950–3953 (1997).
15. Z.-G. Ye, B. Noheda, M. Dong, D. Cox, G. Shirane, Monoclinic phase in the relaxor-based piezoelectric/ferroelectric $Pb(Mg_{1/3}Nb_{2/3})O_3-PbTiO_3$ system. *Phys. Rev. B* **64**, 184114 (2001).
16. G. Xu, Z. Zhong, Y. Bing, Z.-G. Ye, C. Stock, G. Shirane, Ground state of the relaxor ferroelectric $Pb(Zn_{1/3}Nb_{2/3})O_3$. *Phys. Rev. B* **67**, 104102 (2003).
17. G. Xu, Z. Zhong, H. Hiraka, G. Shirane, Three-dimensional mapping of diffuse scattering in $Pb(Zn_{1/3}Nb_{2/3})O_3-xPbTiO_3$. *Phys. Rev. B* **70**, 174109 (2004).
18. G. Xu, Z. Zhong, Y. Bing, Z.-G. Ye, G. Shirane, Electric-field-induced redistribution of polar nano-regions in a relaxor ferroelectric. *Nat. Mater.* **5**, 134–140 (2006).
19. M. Matsuura, K. Hirota, P. M. Gehring, Z.-G. Ye, W. Chen, G. Shirane, Composition dependence of the diffuse scattering in the relaxor ferroelectric compound $(1-x)Pb(Mg_{1/3}Nb_{2/3})O_3-xPbTiO_3 (0\leq x\leq 0.40)$. *Phys. Rev. B* **74**, 144107 (2006).
20. G. Xu, Probing local polar structures in PZN-*x*PT and PMN-*x*PT relaxor ferroelectrics with neutron and x-ray scattering. *J. Phys. Conf. Ser.* **320**, 012081 (2011).
21. M. J. Krogstad, P. M. Gehring, S. Rosenkranz, R. Osborn, F. Ye, Y. Liu, J. P. C. Ruff, W. Chen, J. M. Wozniak, H. Luo, O. Chmaissem, Z.-G. Ye, D. Phelan, The relation of local order to material properties in relaxor ferroelectrics. *Nat. Mater.* **17**, 718–724 (2018).
22. J. Kim, A. Kumar, Y. Qi, H. Takenaka, P. J. Ryan, D. Meyers, J.-W. Kim, A. Fernandez, Z. Tian, A. M. Rappe, J. M. LeBeau, L. W. Martin, Coupled polarization and nanodomain evolution underpins large electromechanical responses in relaxors. *Nat. Phys.* **18**, 1502–1509 (2022).

23. K. Hirota, Z.-G. Ye, S. Wakimoto, P. M. Gehring, G. Shirane, Neutron diffuse scattering from polar nanoregions in the relaxor $Pb(Mg_{1/3}Nb_{2/3})O_3$. *Phys. Rev. B* **65**, 104105 (2002).
24. K. Ohwada, K. Hirota, P. W. Rehrig, Y. Fujii, G. Shirane, Neutron diffraction study of field-cooling effects on the relaxor ferroelectric $Pb[(Zn_{1/3}Nb_{2/3})_{0.92}Ti_{0.08}]O_3$. *Phys. Rev. B* **67**, 094111 (2003).
25. D. La-Orauttapong, J. Toulouse, Z.-G. Ye, W. Chen, R. Erwin, J. L. Robertson, Neutron scattering study of the relaxor ferroelectric $(1-x)Pb(Zn_{1/3}Nb_{2/3})O_3-xPbTiO_3$. *Phys. Rev. B* **67**, 134110 (2003).
26. G. Xu, G. Shirane, J. R. D. Copley, P. M. Gehring, Neutron elastic diffuse scattering study of $Pb(Mg_{1/3}Nb_{2/3})O_3$. *Phys. Rev. B* **69**, 064112 (2004).
27. F. Bai, N. Wang, J. Li, D. Viehland, P. M. Gehring, G. Xu, G. Shirane, X-ray and neutron diffraction investigations of the structural phase transformation sequence under electric field in $0.7Pb(Mg_{1/3}Nb_{2/3})$-$0.3PbTiO_3$ crystal. *J. Appl. Phys.* **96**, 1620–1627 (2004).
28. A. K. Singh, D. Pandey, O. Zaharko, Powder neutron diffraction study of phase transitions in and a phase diagram of $(1-x)[Pb(Mg_{1/3}Nb_{2/3})O_3]-xPbTiO_3$. *Phys. Rev. B* **74**, 024101 (2006).
29. P. M. Gehring, Neutron diffuse scattering in lead-based relaxor ferroelectrics and its relationship to the ultra-high piezoelectricity. *J. Adv. Dielectr.* **02**, 1241005 (2012).
30. D. Phelan, E.E. Rodriguez, J. Gao, Y. Bing, Z.-G. Ye, Q. Huang, J. Wen, G. Xu, C. Stock, M. Matsuura, P.M. Gehring, Phase diagram of the relaxor ferroelectric $(1-x)Pb(Mg_{1/3}Nb_{2/3})O_3+xPbTiO_3$ revisited: a neutron powder diffraction study of the relaxor skin effect. *Phase Transitions* **88**, 283–305 (2015).
31. B. Burton, E. Cockayne, U. Waghmare, Correlations between nanoscale chemical and polar order in relaxor ferroelectrics and the lengthscale for polar nanoregions. *Phys. Rev. B* **72**, 064113 (2005).
32. G. Xu, J. Wen, C. Stock, P. M. Gehring, Phase instability induced by polar nanoregions in a relaxor ferroelectric system. *Nat. Mater.* **7**, 562–566 (2008).
33. M. E. Manley, D. L. Abernathy, Raffi Sahul, D. E. Parshall, J. W. Lynn, A. D. Christianson, P. J. Stonaha, E. D. Specht, J. D. Budai, Giant electromechanical coupling of relaxor ferroelectrics controlled by polar nanoregion vibrations. *Sci. Adv.* **2**, e1501814 (2016).
34. F. Li, S. Zhang, T. Yang, Z. Xu, N. Zhang, G. Liu, J. Wang, J. Wang, Z. Cheng, Z.-G. Ye, J. Luo, T. R. Shrout, L.-Q. Chen, The origin of ultrahigh piezoelectricity in relaxor-ferroelectric solid solution crystals. *Nat. Commun.* **7**, 13807 (2016).
35. F. Li, S. Zhang, Z. Xu, L.-Q. Chen, The Contributions of Polar Nanoregions to the Dielectric and Piezoelectric Responses in Domain-Engineered Relaxor-$PbTiO_3$ Crystals. *Adv. Funct. Mater.* **27**, 1700310 (2017).
36. H. Takenaka, I. Grinberg, S. Liu, A. M. Rappe, Slush-like polar structures in single-crystal relaxors. *Nature* **546**, 391–395 (2017).
37. W.-Y. Chang, C.-C. Chung, Z. Yuan, C.-H. Chang, J. Tian, D. Viehland, J.-F. Li, J. L. Jones, X. Jiang, Patterned nano-domains in PMN-PT single crystals. *Acta Mater.* **143**, 166–173 (2018).
38. A. Kumar, J. N. Baker, P. C. Bowes, M. J. Cabral, S. Zhang, E. C. Dickey, D. L. Irving, J. M. LeBeau, Atomic-resolution electron microscopy of nanoscale local structure in lead-based relaxor ferroelectrics. *Nat. Mater.* **20**, 62–67 (2021).
39. Z.-G. Ye, Crystal chemistry and domain structure of relaxor piezocrystals. *Curr. Opin. Solid State Mater. Sci.* **6**, 35–44 (2002).
40. V. V. Shvartsman, B. Dkhil, A. L. Kholkin, Mesoscale Domains and Nature of the Relaxor State by Piezoresponse Force Microscopy. *Annu. Rev. Mater. Res.* **43**, 423–449 (2013).
41. V. V. Shvartsman, A. L. Kholkin, Polar structures of $PbMg_{1/3}Nb_{2/3}O_3$-$PbTiO_3$ relaxors: piezoresponse force microscopy approach. *J. Adv. Dielectr.* **02**, 1241003 (2012).
42. F. Li, S. Zhang, D. Damjanovic, L.-Q. Chen, T. R. Shrout, Local Structural Heterogeneity and Electromechanical Responses of Ferroelectrics: Learning from Relaxor Ferroelectrics. *Adv. Funct. Mater.* **28**, 1801504 (2018).
43. R. P. Winarski, M. V. Holt, V. Rose, P. Fuez, D. Carbaugh, C. Benson, D. Shu, D. Kline, G. B. Stephenson, I. McNulty, J. Maser, A hard X-ray nanoprobe beamline for nanoscale microscopy. *J. Synchrotron Radiat.* **19**, 1056–1060 (2012).
44. J. Kim, H. Takenaka, Y. Qi, A. R. Damodaran, A. Fernandez, R. Gao, M. R. McCarter, S. Saremi, L. Chung, A. M. Rappe, L. W. Martin, Epitaxial Strain Control of Relaxor Ferroelectric Phase Evolution. *Adv. Mater.* **31**, 1901060 (2019).
45. J. C. Ho, K. S. Liu, I. N. Lin, Study of ferroelectricity in the PMN-PT system near the morphotropic phase boundary. *J. Mater. Sci.* **28**, 4497–4502 (1993).
46. Material synthesis and data analysis methods are available as Supplementary Materials.
47. Y.-H. Chu, Q. Zhan, L. W. Martin, M. P. Cruz, P.-L. Yang, G. W. Pabst, F. Zavaliche, S.-Y. Yang, J.-X. Zhang, L.-Q. Cheng, D. G. Schlom, I.-N. Lin, T.-B. Wu, R. Ramesh, Nanoscale Domain Control in Multiferroic $BiFeO_3$ Thin Films. *Adv. Mater.* **18**, 2307–2311 (2006).

48. M. Otoničar, A. Bradeško, L. Fulanović, T. Kos, H. Uršič, A. Benčan, M. J. Cabral, A. Henriques, J. L. Jones, L. Riemer, D. Damjanovic, G. Dražić, B. Malič, T. Rojac, Connecting the multiscale structure with macroscopic response of relaxor ferroelectrics. *Adv. Funct. Mater.* **30**, 2006823 (2020).
49. R. Xu, S. Liu, I. Grinberg, J. Karthik, A. R. Damodaran, A. M. Rappe, & L. W. Martin, Ferroelectric polarization reversal via successive ferroelastic transitions. *Nat. Mater.* **14**, 79-86 (2015).
50. K. L. Kim, N. T. Tsou, J. E. Huber, Domain evolution processes during poling of a near-morphotropic Pb(Zr, Ti)O_3 ceramic. *J. Appl. Phys.* **113**, 194104 (2013).
51. Y. Yan, L. Yang, Y. Zhou, K.-H. Cho, J. S. Heo, S. Priya, Enhanced temperature stability in <111> textured tetragonal Pb($Mg_{1/3}Nb_{2/3}$)O_3-$PbTiO_3$ piezoelectric ceramics. *J. Appl. Phys.* **118**, 104101 (2015).
52. P. S. Bednyakov, B. I. Sturman, T. Sluka, A. K. Tagantsev, P. V. Yudin, Physics and applications of charged domain walls. *npj Comput. Mater.* **4**, 65 (2018).
53. H. Fu, R. E. Cohen, Polarization rotation mechanism for ultrahigh electromechanical response in single-crystal piezoelectrics. *Nature* **403**, 281–283 (2000).
54. L. W. Martin, A. M. Rappe, Thin-film ferroelectric materials and their applications. *Nat. Rev. Mater.* **2**, 16087 (2016).
55. L. W. Martin, Y.-H. Chu, R. Ramesh, Advances in the growth and characterization of magnetic, ferroelectric, and multiferroic oxide thin films. *Mater. Sci. Eng.: R: Rep.* **68**, 89–133 (2010).
56. P. Sharma, T. S. Moise, L. Colombo, J. Seidel, Roadmap for Ferroelectric Domain Wall Nanoelectronics. *Adv. Funct. Mater.* **32**, 2110263 (2022).

Acknowledgments
We acknowledge helpful discussions with Dr. Daniel Phelan at the Argonne National Laboratory and Prof. Wanzheng Hu of the University of Boston. Y. C. and T.D.F. thank Jonathan Karsch at the University of Chicago for helping with the PMN-0.32PT device at the early stage of the experiment.

Funding: The coherent X-ray experiment, data analysis, and interpretation at the Argonne National Laboratory were supported by the U.S. Department of Energy, Office of Science, Basic Energy Sciences, Materials Science and Engineering Division. This research used resources of the Advanced Photon Source, a U.S. Department of Energy (DOE) Office of Science User Facility operated for the DOE Office of Science by Argonne National Laboratory under Contract No. DE-AC02-06CH11357. Work performed at the Center for Nanoscale Materials, a U.S. Department of Energy Office of Science User Facility, was supported by the U.S. DOE, Office of Basic Energy Sciences, under Contract No. DE-AC02-06CH11357. The synthesis of complex oxide films for these driven studies was supported by the U.S. Department of Energy, Office of Science, Office of Basic Energy Sciences, under Award Number DE-SC-0012375. Jie.K. acknowledges the support of the Army/DEVCOM/ARL via the Collaborative for Hierarchical Agile and Responsive Materials (CHARM) under cooperative agreement W911NF-19-2-0119. Jiy.K. acknowledges the support of the Army Research Office under Grant W911NF-21-1-0118. L.W.M. acknowledges additional support from the National Science Foundation under Grant DMR-2102895.

Author contributions
Y.C. conceived the idea and the project plan. H.Z., D.S., T.D.F. Y.C. conducted X-ray nanodiffraction experiments. H.Z. conducted X-ray RSM. Jie.K and Jiy.K synthesized the samples and performed characterizations on their physical properties. H.Z. performed experimental data analyses; T.Z. extensively helped in the simulation of nanodiffraction reflections. All authors participated in discussions. H.Z. and Y.C. prepared the manuscript with input from all authors.

Competing interest
The authors declare no competing interests.

Data and material availability:
All data needed to evaluate the conclusions in this work are presented in the paper and/or the Supplementary Materials. The simulation and analysis are freely available at Zenodo (10.5281/zenodo.10957580).